

Article

Facile Synthesis of Heterogeneous Indium Nanoparticles for Formate Production via CO₂ Electroreduction

Ana Cristina Pérez-Sequera ¹, Manuel Antonio Diaz-Perez ¹, Mayra Anabel Lara Angulo ¹, Juan P. Holgado ² and Juan Carlos Serrano-Ruiz ^{1,*}

¹ Materials and Sustainability Group, Department of Engineering, Universidad Loyola Andalucía, Avda. de las Universidades s/n, 41704 Dos Hermanas, Spain

² Instituto de Ciencia de Materiales de Sevilla and Departamento de Química Inorgánica, CSIC-Univ de Sevilla, Av. Américo Vespucio, 49, 41092 Seville, Spain

* Correspondence: jcserrano@uloyola.es

Abstract: In this study, a simple and scalable method to obtain heterogeneous indium nanoparticles and carbon-supported indium nanoparticles under mild conditions is described. Physicochemical characterization by X-ray diffraction (XRD), X-ray photoelectron microscopy (XPS), scanning electron microscopy (SEM) and transmission electron microscopy (TEM) revealed heterogeneous morphologies for the In nanoparticles in all cases. Apart from In⁰, XPS revealed the presence of oxidized In species on the carbon-supported samples, whereas these species were not observed for the unsupported samples. The best-in-class catalyst (In₅₀/C₅₀) exhibited a high formate Faradaic efficiency (FE) near the unit (above 97%) at −1.6 V vs. Ag/AgCl, achieving a stable current density around −10 mA·cm_{geo}^{−2}, in a common H-cell. While In⁰ sites are the main active sites for the reaction, the presence of oxidized In species could play a role in the improved performance of the supported samples.

Keywords: indium catalysts; CO₂ electroreduction; carbon-supported materials; heterogeneous catalysts; formate production; CO₂ conversion



Citation: Pérez-Sequera, A.C.; Diaz-Perez, M.A.; Lara Angulo, M.A.; Holgado, J.P.; Serrano-Ruiz, J.C. Facile Synthesis of Heterogeneous Indium Nanoparticles for Formate Production via CO₂ Electroreduction. *Nanomaterials* **2023**, *13*, 1304. <https://doi.org/10.3390/nano13081304>

Academic Editor: Adriano Sacco

Received: 30 January 2023

Revised: 29 March 2023

Accepted: 3 April 2023

Published: 7 April 2023



Copyright: © 2023 by the authors. Licensee MDPI, Basel, Switzerland. This article is an open access article distributed under the terms and conditions of the Creative Commons Attribution (CC BY) license (<https://creativecommons.org/licenses/by/4.0/>).

1. Introduction

The ever-increasing human population growth rate has increased the world energy demand, leading to higher CO₂ emissions since a high percentage of the energy demand is still supported by fossil fuels [1]. The unceasing rise of the concentration of carbon dioxide, a powerful greenhouse gas, into the atmosphere is affecting the natural systems balance, leading to an acceleration of global warming [2]. In order to mitigate the impact of carbon dioxide emissions, several technologies have been developed [3–7]. Among them, electrochemical techniques able to upgrade carbon dioxide to value added chemicals have demonstrated to be a promising solution owing to their mild operating conditions and good performance [8]. By means of the electrochemical carbon dioxide reduction reaction (CO₂RR), CO₂ dissolved in aqueous medium can be converted into fuels and value-added chemicals [9], including carbon monoxide (CO), methanol (CH₃OH), methane (CH₄) and formic acid/formate (CHOOH), and even C₂₊ products such as ethanol (CH₃CH₂OH), acetic acid (CH₃COOH), ethylene (C₂H₄) and n-propanol (CH₃CH₂CH₂OH) [10–13]. Formic acid, an important chemical thoroughly employed in the industry, has gained a great attention recently due its potential use as hydrogen storage compound in fuel cells applications [14]. However, the production of formic acid is limited by a sluggish kinetic due to the high energy required to activate the CO₂ molecule to the intermediate CO₂^{•−}. Moreover, the hydrogen evolution reaction (HER) represents another limitation due to its competitive equilibrium onset potential (close to that of CO₂RR), leading to low products selectivities [15,16]. To overcome these barriers, highly active, stable and selective catalysts capable of suppressing HER are necessary [17–19]. In this sense, low toxicity and environmentally

friendly transition metals such as indium (In) have demonstrated good electrocatalytic behavior as cathode material in the CO₂RR since they combine high HER overpotentials and good selectivity to formate [20]. Nevertheless, indium-based materials typically present low current densities at low overpotentials and poor stability, exhibiting electrocatalytic activity decays after 2 h of electrolysis [21]. Hence, to improve the electrocatalytic performance and considering the rich structure sensitivity of the CO₂RR, engineered indium-based catalysts have been synthesized with diverse shapes and morphologies including nanoparticles [22], nanocrystals [23], nanobelts [24], nanosheets [25], nanowires [26], nanocubes [27] and dendrites [28–30]. Thus, the morphology and shape of the indium particles can determine the number of edges, corners and plain sites, which can lead to enhancements on the activity, selectivity, stability and electronic properties [21,27]. Furthermore, the performance of the catalytic materials can be also improved by generating heterostructures or the introduction of structure defects (e.g., vacancies). These defects can modify the electronic properties of the catalyst surface, resulting in lower energy barriers [31–34]. For instance, Yang et al. achieved enhanced CO₂RR activity by generating structure defects on synthesized In/In oxide heterostructures, resulting in formate selectivities as high as 93% at -0.9 V vs. reversible hydrogen electrode (RHE) in a 0.5 M KHCO₃ solution [35]. Abundant carbon-based materials with tunable morphology, large surface area, porosity and high mechanical stability are optimal metal supports for the CO₂RR [21,36]. In this regard, Rabiee et al. achieved high faradaic efficiencies (FE) to formate (70–77%) at -1.6 V vs. SCE in 0.5 K₂SO₄ over In(OH)₃ nanocubic mesoporous particles supported on carbon black [27]. Despite the latest advances made in the development of active In catalysts for the CO₂RR, the synthesis routes employed often consist on several complex steps under nonstandard conditions, thereby hindering scale up to industrial applications. Thus, it is highly desirable to develop catalyst synthesis methodologies with low complexity to ensure the economic viability of the overall process.

In this work, we describe a facile synthesis procedure to obtain indium nanoparticles (In NPs) and carbon-supported In NPs, and their performance was evaluated as CO₂RR cathodes. In NPs were synthesized by a simple two-step method and subsequently washed with different mild reagents with the aim to optimize the behavior of the material. Moreover, In NPs were supported on carbon black at different mass ratios (In₂₀/C₈₀ and In₅₀/C₅₀). The as-obtained NPs were fully characterized by physicochemical techniques such as X-ray diffraction (XRD), X-ray photoelectron spectroscopy (XPS), scanning electron microscopy (SEM), transmission electron microscopy (TEM) and high-resolution TEM (HR-TEM). In addition, electrochemical techniques such as cyclic voltammetry and bulk electrolysis were applied to study the electroactivity of the catalysts in the CO₂RR. The optimum catalyst obtained by the proposed method (In₅₀/C₅₀) achieved a stable current density above -10.6 mA·cm_{geo}⁻² at -1.6 V vs. Ag/AgCl with a formate FE as high as 97%. The presence of surface oxidized species and the support-catalyst interactions could be related with the superior behavior of this catalyst. Our results provide an easy and affordable synthetic methodology to produce highly efficient and stable indium-based nanoparticles with excellent formate selectivity.

2. Materials and Methods

2.1. Reagents and Materials

Indium (III) chloride (InCl₃, 99.999%), polyvinylpyrrolidone (PVP, K30, M_w~55.000), sodium borohydride (NaBH₄, 99%), Nafion™ perfluorinated resin solution dispersion (5 wt. % in mixture of lower aliphatic alcohols and water) and indium foil (CAS N° 744-74-6, 0.1 mm thickness, 99.995% purity) were purchased from Sigma-Aldrich Co. Potassium hydrogen carbonate (KHCO₃, 99.5–101%), potassium chloride (KCl, 99.5–100.5%) and ethanol (C₂H₅OH, 96%) were purchased from PanReac. Potassium hydroxide (KOH, 85%) and ethanol absolute (C₂H₅OH, 98.8%) were purchased from Labkem. Vulcan XC-72 carbon powder (CAS N° 1333-86-4, N° 215-609-9) was purchased from FullCellStore. Nylon membrane filter (90 mm, 0.22 μm, Cod.MNY022090N) was purchased from FILTER-LAB®.

Cationic ion exchange membrane NafionTM 115 (CAS31175-20-9) was also purchased from Sigma-Aldrich. Carbon fiber paper TorayTM (TP-90) was purchased from QuinTech. All chemicals were purchased with the highest analytical grade available and were employed without any further purification. All the solutions were prepared using MilliQ ultra-pure deionized water (DIW, $18.2 \text{ MW}\cdot\text{cm}^{-1}$ of resistivity) to avoid the presence of any trace metal impurities from water which could affect the CO₂RR performance.

2.2. Synthesis Procedures

2.2.1. In NPs Synthesis

In NPs were synthesized by modifying a simple two-step hydrothermal method [37]. Briefly, 0.110 g of the metallic precursor (InCl₃) and 1 g of the capping agent (PVP) were dissolved in pure water at 60 °C under vigorous stirring for 30 min. Then, 0.230 g of the reductant agent (NaBH₄), previously dissolved in cold DI water, was added to the solution, exposing an abrupt color change from translucent to dark grey as a result of the reduction of the metal particles. The resultant solution was maintained under continuous stirring and alternated with 3 min of sonication for another 30 min. Once a homogeneous solution is obtained, 50 mL of ethanol (96%) were added for inducing the precipitation of the particles. This step was repeated two times. The as-obtained product is filtered with a nylon membrane filter and washed with an ethanol/potassium hydroxide (0.1 M) solution (50/50 vol. %) or DI water/ethanol solution (50/50 vol%), depending on the catalyst batch prepared. The selection of these two different washing solutions was tested as route to optimize the cleaning step. Finally, the obtained wet powder was vacuum dried at 50 °C for 8 h. The as-obtained NPs were denoted as In_{H₂O} and In_{KOH}, respectively.

2.2.2. In_x/C_y Synthesis

In_x/C_y NPs were synthesized using a similar methodology. Once the reductant agent is completely dissolved into the solution containing the indium precursor and the PVP (approximately after 30 min of continuous stirring), a proper amount of Vulcan XC-72 carbon powder was added to the mixture. Nominal metal loadings of 20 wt. % and 50 wt. %, respect to the carbon support were achieved and denoted as In₂₀/C₈₀ and In₅₀/C₅₀, respectively. Once the final suspension was stirred for 30 min and then sonicated for another 30 min, 50 mL of ethanol (96%) were added. Finally, the so-synthesized nanoparticles were filtered and washed with the same mixture of ethanol/potassium hydroxide and dried as described in the previous section.

2.2.3. Catalytic ink and Working Electrodes Preparation

For the preparation of the In-based electrodes, a catalytic ink was firstly prepared by dispersing the In NPs in a Nafion solution (perfluorinated resin solution 5 wt.%) serving as a binder factor, with a catalyst/nafion mass ratio of 70:30 and diluted to 2 wt. % in absolute ethanol (98.8%). The solution was sonicated for 60 min and sprayed over a carbon paper (TP-090, QuinTech) by means of an air brushing technique. To promote the deposit of uniform layers of ink on the cathode, the carbon substrate was set between two iron plaques placed on a hot plate at 110 °C to allow fast evaporation of the solvent. The catalytic area of the electrodes was 9 cm² with the same mass loading in all of them of 0.8 mg·cm_{geo}⁻² of In.

2.3. Physicochemical Characterization of Materials

XRD was carried out to identify the existence of crystalline phases in the samples. Patterns were recorded on a Linxeye-XE-D8-Advance spectrometer with a Cu-K α radiation (1.54060 Å) and a source operating at 40 kV and 40 mA. To evaluate the surface morphology of the NPs, SEM was performed on a Hitachi-S4800 microscope operating at 0.5–30 kV. The average size of nanoparticles and plane spacing was study in detail by means of TEM and HR-TEM. The measurements were performed by a JEOL 2100Plus microscope operated at 200 kV, coupled with a EDX X-Max 80 T (Oxford Instruments). To detect the surface states of the metallic nanoparticles, XPS measurements were carried out in a customized system

incorporating a hemispherical analyzer (SPECS Phoibos 150) and a non-monochromatized X-ray source (Al K α , 1486.6 eV; Mg K α , 1253.6 eV), working at 14.0 Kv of anode voltage and 14.4 anode current (200 W). The analyzer was operated at a fixed transmission and 20 eV pass energy with an energy step of 0.1 eV.

2.4. Electrochemical Characterization

The electrochemical tests were carried out at ambient temperature in a custom-made, two compartment sealed H-cell, separated by a proton exchange membrane (Nafion 115). The catholyte compartment was filled with 140 mL of a 0.5 M KHCO₃ and 0.45 M KCl solution, continuously bubbled with Ar or CO₂, during the cyclic voltammetry measurements. A constant purge of CO₂ was maintained during the electrolysis experiments to keep CO₂ saturation and solution convection. The current densities obtained were normalized by the catalytic geometric area of the working electrodes (3 cm² for In-based cathodes). A commercial AgCl/Ag (3.5 M KCl, Metrohm, Herisau, Switzerland) was used as a reference electrode. The anolyte compartment was filled with a 1 M KOH solution and a nickel mesh was used as counter electrode. Cyclic voltammetry sweep (CVS) and chronoamperometric measurements were carried out by means of a potentiostat PGSTAT302N system (Metrohm Autolab B. V., Utrecht, The Netherlands).

2.5. Products Analysis

Liquid aliquots were collected from the catholyte compartment every 30 min. To measure the formate concentration, we used ion chromatography (Dionex Easion) from the company Thermo Scientific (Waltham, MA, USA) with a suppressed conductivity detection, ASRS self-regenerating suppressor (Dionex ASRS™ 300) and AS23 (Dionex IonPac™ AS23) column. A 4.5 mM Na₂CO₃ and 0.8 mM NaHCO₃ was used as eluent. Formate concentration was obtained using different calibration curves over the 0.2 to 24 ppm range. FE for formate was calculated as:

$$FE(\%) = \frac{z \cdot F \cdot n}{Q} \cdot 100, \quad (1)$$

where z is the number of electrons exchanged for the reduction of CO₂ to formate, F is the Faraday constant (96.485 C·mol⁻¹), n is the number of formate moles present in the sample, and Q is the total charge transfer.

3. Results and Discussion

3.1. Materials Characterization

3.1.1. XRD Diffraction Patterns and XPS Spectra

The crystal structures of the as-synthesized samples were determined by XRD analyses. Figure 1a shows the diffraction patterns of the bulk In catalysts washed with H₂O and KOH (In_{H₂O} and In_{KOH}, respectively), and In supported on carbon catalysts at different ratios (In₂₀/C₈₀ and In₅₀/C₅₀). All the samples analyzed exhibited sharp and well defined peaks at 32.96, 36.35, 39.14, 54.55, 56.53, 63.20, 67.01 and 69.07°, which, respectively, corresponded with the (101), (002), (110), (112), (200), (103), (211) and (202) crystallographic planes of a tetragonal crystalline phase of metallic In (COD:96-210-0457) [38–40]. As can be observed, the most intense peak was associated with the plane (101) of In, revealing that this plane was the most abundant in the In NPs in all cases [31]. Besides the sharp XRD peaks, a trace amounts of some impurities can be observed in the bulk In catalyst washed with water (In_{H₂O}), evidenced by the presence of a wide and low intensity peak at ca. 20°.

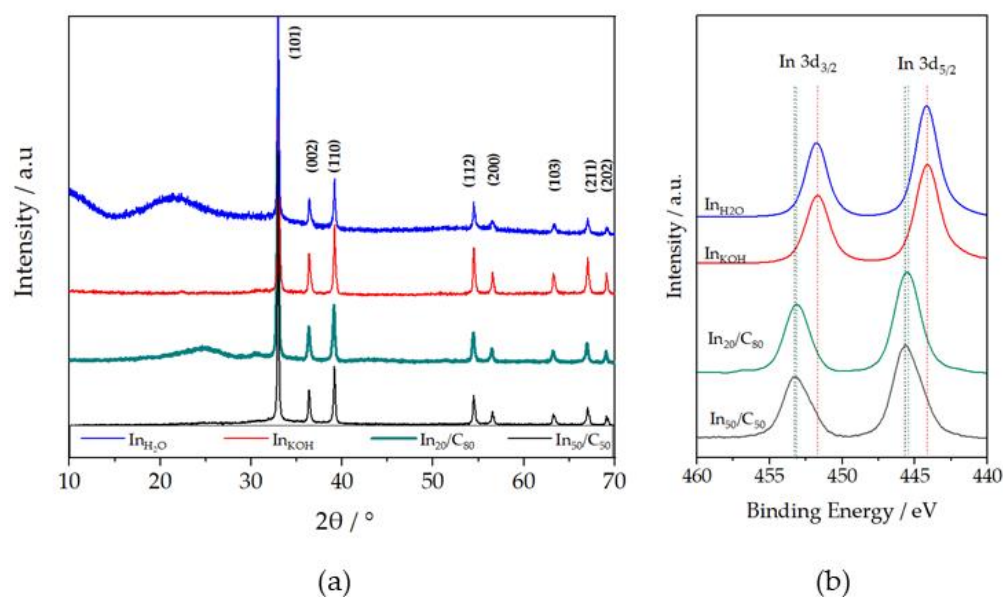


Figure 1. (a) X-ray diffraction patterns of $\text{In}_{\text{H}_2\text{O}}$, In_{KOH} , $\text{In}_{20}/\text{C}_{80}$ and $\text{In}_{50}/\text{C}_{50}$ NPs, with lattice planes identification of mayor peaks [38,39]; (b) XPS spectra of In 3d for In_{KOH} , $\text{In}_{20}/\text{C}_{80}$ and $\text{In}_{50}/\text{C}_{50}$ NPs.

The broad peak at ca. 25° in the XRD pattern of $\text{In}_{20}/\text{C}_{80}$ can be ascribed to the (002) plane of C, in line with previous works [38,41,42]. On the other hand, the average crystal sizes of the catalysts were obtained from Scherrer's equation [43]. The crystallite size obtained were 59.3 nm, 68.6 nm, 42.5 nm and 54.9 nm for $\text{In}_{\text{H}_2\text{O}}$, In_{KOH} , $\text{In}_{20}/\text{C}_{80}$ and $\text{In}_{50}/\text{C}_{50}$ NPs, respectively.

To compare the composition of the catalysts surface of unsupported and supported, XPS analyses were carried out. The samples unsupported, $\text{In}_{\text{H}_2\text{O}}$ and In_{KOH} , showed a doublet (Figure 1b), corresponding to In 3d_{3/2} and In 3d_{5/2} levels, with maxima for 3d_{5/2} signal at ca. 444.2 eV. On the other hand, $\text{In}_{20}/\text{C}_{80}$ and $\text{In}_{50}/\text{C}_{50}$ exhibited its 3d_{5/2} signal at ca. 445.5 and 445.6 eV, respectively. Although these values are slightly higher than those normally reported for and In^0 (443.8 eV) and In^{3+} (445.0 eV) [44,45], this shift has been also found in some cases [12]. In fact, the calibration has been based on an interactive assignment of the binding energy for In3d peaks, considering reasonable values for that doublet, but a variation of around ± 0.4 eV for In^0 and ± 0.6 eV for In^{3+} could be considered [46,47]. In addition, some binding energies displacement could be considered as consequence of the interactions with the support [48–51]. Therefore, the peaks at 445.5 for $\text{In}_{20}/\text{C}_{80}$ or 445.6 for $\text{In}_{50}/\text{C}_{50}$, and 444.5 eV can be ascribed to In^{3+} and In^0 species, respectively. These results indicate the absence of oxidized species on the $\text{In}_{\text{H}_2\text{O}}$ and In_{KOH} materials, whereas carbon-supported samples contain a significant amount of oxidized In species. Furthermore, the slight displacement between the signals of the supported samples may suggest that $\text{In}_{50}/\text{C}_{50}$ sample contain a higher concentration of oxidized species than $\text{In}_{20}/\text{C}_{80}$, which is logical since the In loading is much higher in the former than in the latter. XPS measurements also revealed the presence of very weak nitrogen signals, which are likely to originate from PVP (Figure S1). The very low intensity of these signals indicate that N is present at trace levels on the surface of the catalysts, suggesting that the synthesis route used herein was effective in removing impurities. Thus, XRD and XPS data seem to point out the presence of In NPs with a surface shell enriched in In^{3+} species (as derived from XPS results) and a core mainly composed on metallic In (as revealed in XRD diffractograms) in carbon-supported materials.

3.1.2. SEM

The morphology of the samples was analyzed by means of SEM. A representative SEM image (Figure 2) shows the presence of diverse morphologies depending on the catalyst. As shown in Figure 2a, $\text{In}_{\text{H}_2\text{O}}$ exhibits a variety of shapes such as spheres, triangles, octahedrons, nanorods-like and also some bulk-like shapes. In_{KOH} in Figure 2b, for its part, also shows the presence of different morphologies, with a predominance of nearly spherical particles. The prevalence of spherical nanoparticles and the presence of triangles and also rod-like particles have been previously reported to be formed in reductive environments, pointing out that the reduction kinetics (represented by the addition rate of the reductant agent), as an influent factor in the shape of the nanocrystals [52]. Moreover, these mixed morphologies have been also reported as a function of synthesis time based on the existence of separate defined nucleation steps with different kinetics. It seems that, in early stages, spherical shapes dominate the particle population with a small presence of triangles but, as the synthesis time advances, the size of the spherical particles grows while the fraction of triangle increases [53]. Likewise, In NPs in the supported materials ($\text{In}_{50}/\text{C}_{50}$ and $\text{In}_{20}/\text{C}_{80}$) also exhibited a variety of shapes but with a higher fraction of spherical nanoparticles as compared to the unsupported samples (Figure 2c,d). It is known that the nature of the support could affect the dispersion of the supported metal and, consequently, its morphology and/or size [51]. In addition, the presence of the carbon support during the chemical reduction process might alter the rates of nucleation and growth of In nanoparticles, thereby favoring the formation of nanospheres versus other morphologies. One of the main factors determining the final morphology and size of metal nanoparticles prepared by the borohydride reduction method (the method used herein) is the rate of addition of the reductive agent. We believe that the presence of a porous material such as carbon might result in borohydride being adsorbed, thereby leading to more controlled and slower addition of the reductive agent to the reaction medium. The same reasoning is valid for the In metal precursor, which is likely to be adsorbed on the carbon material during the synthesis, reducing the available concentration in solution. We believe that these conditions (i.e., low metal precursor concentration and controlled and slow addition of the reductive agent) are particularly favorable for the isotropic growth of In nanoparticles, thereby leading to the formation of spherical shapes. It is worth mentioning that most of previous works reported the formation of unique geometries separately [52,54–57]. The synthesis method described in this work leads to a heterogeneous mixture of geometries, which can be an advantageous way to introduce edges sites and to enrich the catalyst morphology. This, considering the high structure sensitivity of the CO_2RR , could represent a simple way for enhance the performance of the reaction.

3.1.3. TEM

Likewise, the SEM analyses, TEM images also reveal the presence of mostly spherical particles (Figure 3a–e). The average size of the prevailing spherical nanoparticles is similar in all the samples (ca. 35 nm), although slight differences can be observed. The In_{KOH} catalyst showed spherical nanoparticles slightly larger (38.39 nm) than those of the $\text{In}_{\text{H}_2\text{O}}$ catalyst (35.95 nm). This difference could be attributed to the more effectiveness of the potassium hydroxide than water for removing the rest of the synthesis reagents. As was previously described in the XRD section, the sample washed with water exhibit the presence of some impurities remaining. Thus, it could be possible that the hydroxide ion may compete with the capping agent for be absorbed on the particle surface, which could induce an accelerated growth of the crystal by decreasing its surface energy [58]. It is worth mentioning that TEM images also confirmed the presence of difference morphologies. Thus, triangles, nanorods and octahedral particles of ca. 145 nm, 700 nm and 82 nm in size, respectively, can be clearly observed in the In_{KOH} catalyst (Figure 3c). However, as shown in Figure 3b, this sample also contained a significant number of spherical In nanoparticles, which are lower in size compared with the previous ones. While we do not rule out that In nanoparticles with special morphologies (e.g., triangles, nanorods and octahedral) have an

effect on the overall catalytic activity, we believe that this effect is minor compared with that of spherical nanoparticles since they are lower in size and possess a higher fraction of high-energy edge and corner sites. These highly energetic sites have been reported to show higher activity than terrace atoms, which are prevalent in large nanoparticles with other morphologies such as nanorods and triangles [22]. For its part, the average sizes of the spherical nanoparticles of $\text{In}_{20}/\text{C}_{80}$ and $\text{In}_{50}/\text{C}_{50}$ were 30.67 nm and 36.47 nm, respectively. Future studies are necessary to evaluate the possibility of enhancing the electroactivity of the samples by controlling the morphology and size of the In particles. A possible approach could be modifying the addition rate of sodium borohydride and the reaction time, both parameters being reported as main factors involved in the nucleation kinetics under reductive environments [52,53]. Additionally, the smaller size of the $\text{In}_{20}/\text{C}_{80}$ NPs confirms the role of the support on the nucleation mechanism of the indium nanoparticles suggested in the previous section.

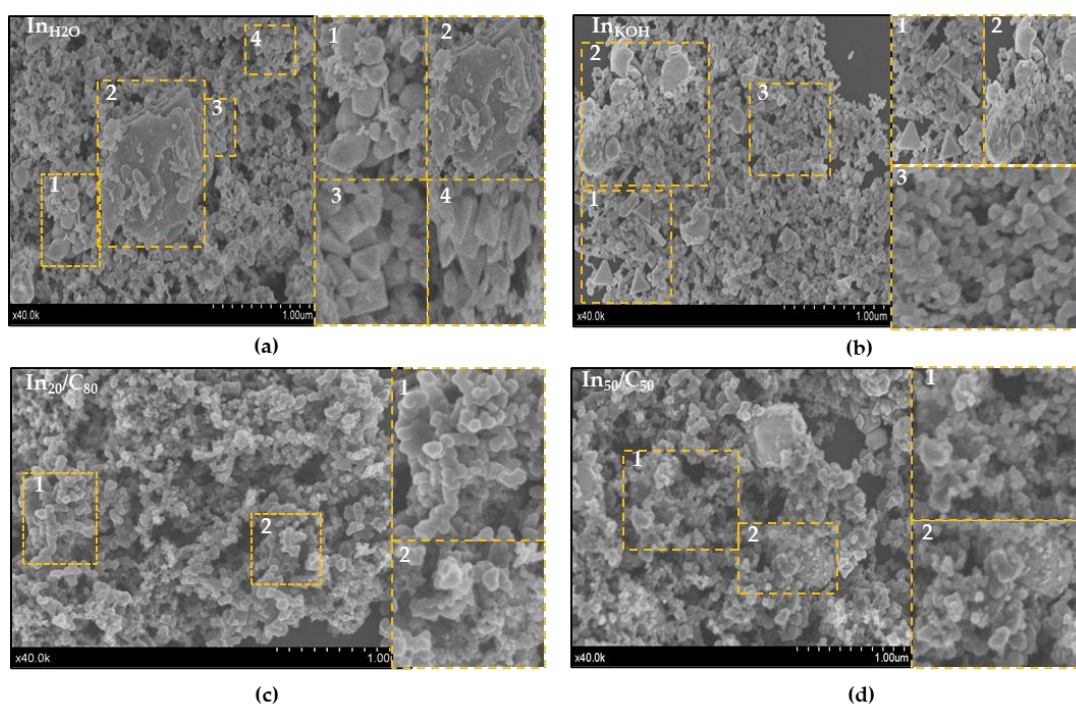


Figure 2. Representative SEM images of: (a) In nanoparticles washed with H_2O ; (b) In nanoparticles washed with KOH . In nanoparticles supported on carbon: (c) 20/80 wt. %; (d) 50/50 wt. %. Some enlargements of the SEM images are included for facilitating the interpretation.

To confirm the presence of oxygenated species (In^{3+}), we analyzed the spherical particles of $\text{In}_{50}/\text{C}_{50}$ by HR-TEM (Figure 4). As shown in Figure 4a, several lattice fringe spacings can be observed around and inside the spheric nanoparticle. In the HR-TEM image, the lattice fringe of 0.279 nm (Figure 4b) can be assigned to the (101) plane of metallic In which is in agreement with that observed by XRD analyses [35]. In addition, the lattice fringes with interplanar spacing of ca. 0.281 nm (Figure 4c) can be indexed to the (220) planes of $\text{In}(\text{OH})_3$ [47,58]. These results confirm the existence of oxygenated species ($\text{In}(\text{OH})_3$) on the catalyst surface, in accordance with that suggested by XPS. Moreover, the element distributions were determined by energy-disperse X-ray spectroscopy (EDX) analyses (Figure 4d). As expected, two intense C and In signals for can be observed since the catalyst is mainly formed by these two elements. In addition, a noticeable peak of O is also evident, revealing the presence of an oxidized phase which may be related with the formation of a thin surface layer [22]. Despite the existence of oxidized species has been probed by XPS and HR-TEM, the signals of $\text{In}(\text{OH})_3$ in the XRD cannot be observed, which can be ascribed to the existence of this specie as an essentially amorphous phase. Hence,

according to XRD, XPS and HR-TEM data, the In over carbon particles are mainly composed by metallic indium along with an oxidized layer at the surface, possibly of $\text{In}(\text{OH})_3$.

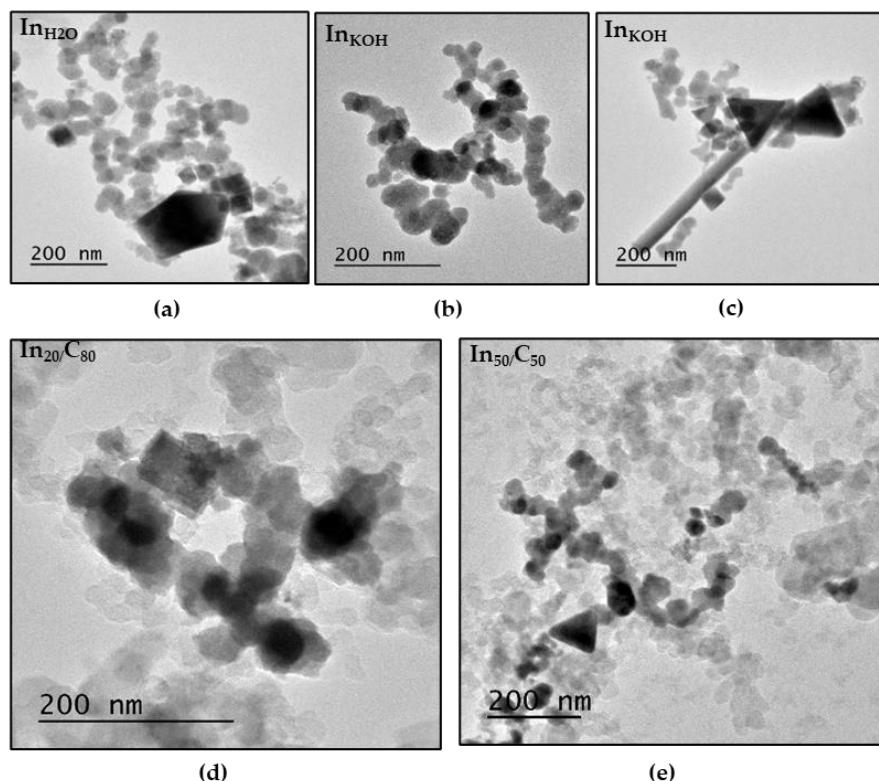


Figure 3. Structural analysis of the nanoparticles by TEM: (a) In NPs washed with H_2O ; (b,c) In NPs washed with KOH; (d) In over carbon with a ratio of 20/80 wt. %. (e) In over carbon with a ratio of 50/50 wt. %.

3.2. Electrochemical Characterization

3.2.1. Effect of the Washing Agents

The electrochemical characterization of the $\text{In}_{\text{H}_2\text{O}}$ and In_{KOH} NPs supported on carbon Toray paper were carried out by means of CVS. The materials were screened between -0.5 V and -1.8 V vs. Ag/AgCl reference electrode, in a H-cell saturated with Ar/ CO_2 with a KHCO_3 0.5 M + KCl 0.45 M solution. Figure 5 shows representative CVS experiments for each material and for an indium foil for sake of comparison, under Ar and CO_2 saturated conditions. Ar-saturated CSV (solid lines) shows the redox pair corresponding with the indium species formed on the interface and the current densities associated with the oxidation/reduction processes. As can be observed (see inset graph in Figure 5), there is an anodic peak which corresponds to the characteristic oxidation of In^0 to In^{3+} at -0.92 V for $\text{In}_{\text{H}_2\text{O}}$, -0.89 V for In_{KOH} and -0.91 V for In foil. The presence of this peak suggests the formation of a passive film of In_2O_3 or $\text{In}(\text{OH})_3$ [38,59]. On the other hand, the reduction of In^{3+} to In^0 can be observed in the negative sweep going at -1.04 V, -0.98 V and -0.99 V, for $\text{In}_{\text{H}_2\text{O}}$, In_{KOH} and In foil, respectively. Additionally, the current densities of the anodic and cathodic peaks for In_{KOH} sample are higher than those obtained for $\text{In}_{\text{H}_2\text{O}}$ NPs, revealing a lower reducibility of In particles in $\text{In}_{\text{H}_2\text{O}}$ as compared to the In_{KOH} catalyst [22]. Furthermore, it is well known that, as the potential shifts to more negative values, the hydrogen evolution reaction (HER), which competes with CO_2RR , becomes more pre-dominant. As shown in Figure 5, under Ar conditions, the In foil electrode showed higher current densities than the In_{KOH} and $\text{In}_{\text{H}_2\text{O}}$ samples at low voltages (-1.4 V and lower), indicating a higher activity of the foil sample towards the HER. These results are in line with previous works revealing In foil to be particularly active in promoting the HER versus CO_2RR [22,35,59]. In terms of onset potentials, the In foil sample showed more

positive values (-1.4 V) than the In_{KOH} (-1.7 V) and $\text{In}_{\text{H}_2\text{O}}$ (-1.8 V) samples, which is also in agreement with the foil sample having a higher HER activity.

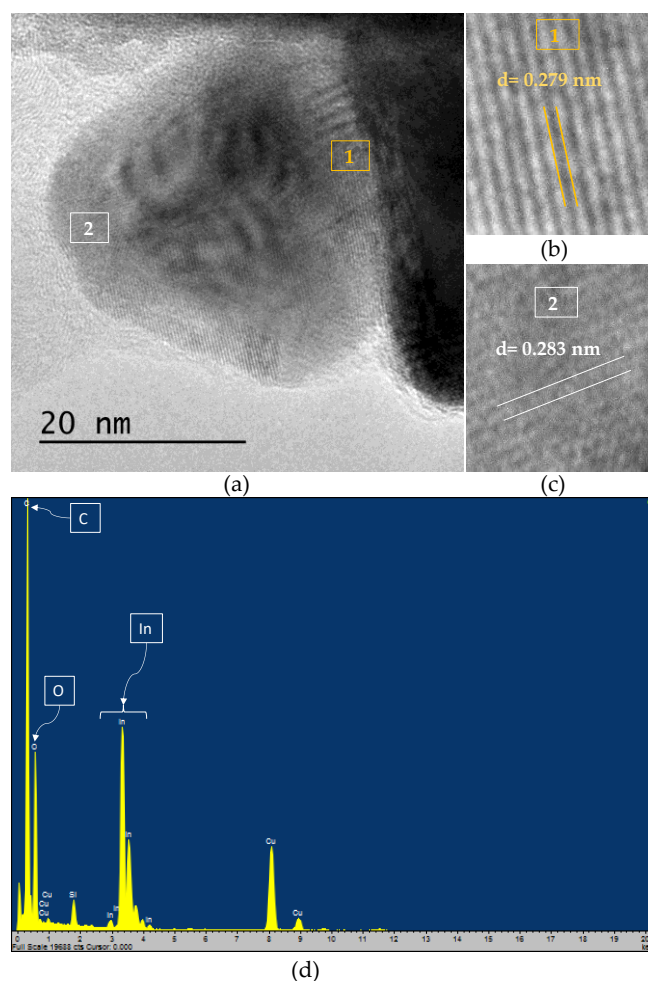


Figure 4. (a) HR-TEM micrograph of $\text{In}_{50}/\text{C}_{50}$ nanoparticles; (b,c) detail of lattice fringe spacings on spherical nanoparticles; (d) EDX pattern showing the elemental composition of the nanoparticles.

On the other hand, the CO_2RR performance of In_{KOH} , $\text{In}_{\text{H}_2\text{O}}$ and the In foil has been evaluated in a solution saturated with CO_2 on the potential range from -1.15 V to -1.8 V (represented with dashes in Figure 5). The change in the pH once CO_2 saturates the solution ($\text{pH}_{\text{CO}_2} = 7.42$) in contrast to that when using Ar ($\text{pH}_{\text{Ar}} = 9.33$), results in a shift to more negative potentials at which the reduction processes take place. Thus, the reduction onset potentials for In_{KOH} , $\text{In}_{\text{H}_2\text{O}}$ and In foil were -1.35 V, -1.42 V and -1.25 V vs. Ag/AgCl, respectively [22,38]. In_{KOH} NPs reached the highest current density at -1.8 V vs. Ag/AgCl ($-15.20 \text{ mA}\cdot\text{cm}_{\text{geo}}^{-2}$) as compared to that obtained by $\text{In}_{\text{H}_2\text{O}}$ ($-12.08 \text{ mA}\cdot\text{cm}_{\text{geo}}^{-2}$) and the In foil ($-10.71 \text{ mA}\cdot\text{cm}_{\text{geo}}^{-2}$). In nanoparticles washed with KOH exhibit a better performance than pure In foil, despite the former has a much lower metallic loading, due principally to the active surface area of the nanoparticles is greater than the bulk material. This promotes contact between the catalyst and the reactants, leading to an enhanced CO_2 reduction. In addition, In_{KOH} NPs also exhibit a larger current density and a lower onset potential than the $\text{In}_{\text{H}_2\text{O}}$ NPs. Despite the clear environmental advantages derived from the use of water, it seems that it is necessary to use a more “aggressive” washing agent than just pure H_2O to clean completely the catalyst surface. As previously commented, XRD results showed that some impurities remain in the In NPs when water was used during the washing step and that could hinder the electroactivity of these nanoparticles. At the

same time, some big conglomerates are observed in SEM images, which will also affect negatively the electroactivity of the material.

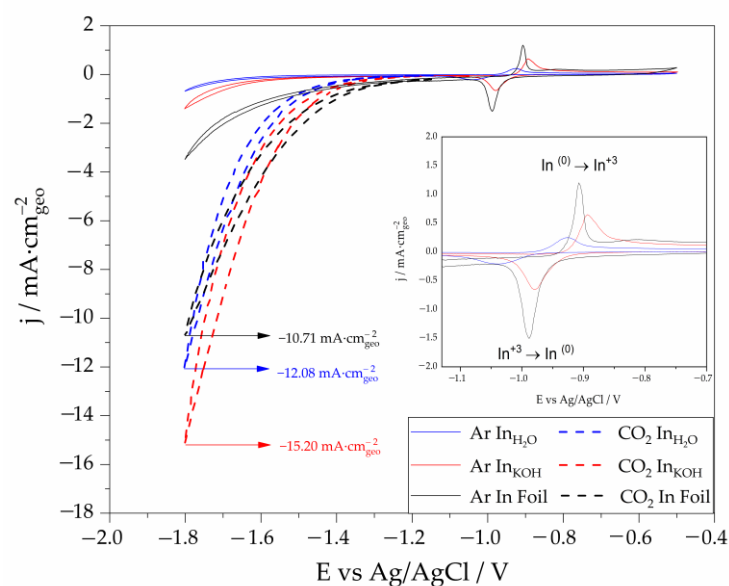


Figure 5. Cyclic voltammograms obtained in Ar (solid lines) and CO₂ (dashed lines) saturated solutions (KHCO₃ 0.5 M + KCl 0.45 M) for In_{H2O}, In_{KOH} and In foil electrodes. Scan rate 50 mV·s⁻¹.

3.2.2. Effect of the Carbon Support

Based on the results obtained from the comparison of the effectiveness of the washing agents, In nanoparticles washed with KOH were supported on carbon Vulcan following the synthesis method described previously. To study the effect of supporting In on carbon, two different catalysts were electrochemically characterized, In₂₀/C₈₀ (Figures 6a and S3a) and In₅₀/C₅₀ (Figures 6b and S3b). As expected, the experiments carried out with Ar (solid line) showed the characteristic patterns for the oxidation (positive going sweep) and for the reduction (negative going sweep) of indium species. In₂₀/C₈₀ catalyst response under Ar saturation conditions shows an anodic peak at -0.88 V and a cathodic peak at -1.10 V. However, In₅₀/C₅₀ electrode displayed two anodic peaks at -0.69 and -0.87 V, unlike In_{KOH} and In₂₀/C₈₀. The peak at -0.87 V corresponds to the oxidation of In⁰ to In⁺³ species, while the peak at -0.69 V may be associate to the presence of In⁺ as a product of an intermediate kinetic step. This may suggest that In₅₀/C₅₀ NPs exhibit a lower kinetic response than those of In_{KOH} and In₂₀/C₈₀ NPs at the same potential window [60–62]. On the other hand, for CO₂ saturated solutions, the electrochemical response of the catalysts supported on carbon, in terms of current density, is more than double of those obtained for unsupported catalysts at -1.8 V vs. Ag/AgCl (see Table 1). This behavior can be attributed to a higher double layer capacitance (cdl) of the carbon-supported samples (Figure S2 and Table S1). Thus, the carbon-supported samples showed higher cdl values (26.5 and 6.4 mF·cm⁻² for In₂₀/80 and In₅₀/50, respectively) than the unsupported In_{KOH} (0.05 mF·cm⁻²). The presence of porous carbon, thanks to its high ratio surface/volume, can increase the capacitance of the double layer, resulting in higher charge-storage capacities at the interface and improved CO₂RR performance [63]. However, the large increase in activity of the In₅₀/C₅₀ catalyst could be ascribed to the presence of an oxidized layer on the catalyst. The higher concentration of In(OH)₃ at the surface in the In₅₀/C₅₀ (see XPS and HR-TEM results) would explain the better CO₂RR performance of this catalyst over the rest of them (see summary Table 1.) [22]. Oxidized metal species have been previously reported to promote both the activity and selectivity in CO₂RR by facilitating proton transfer steps [35,64]. With regard to indium catalysts, In⁰, In₂O₃ and In(OH)₃ have been proposed as the actual active sites for CO₂RR [21,22]. The improved electroactivity of these materials was ascribed to the formation of carbonate species by the interaction of CO₂ with the

surface oxidized layer [65]. Surface In^{+3} species (e.g., $\text{In}(\text{OH})_3$) have been reported to allow the chemisorption of CO_2 via formation of In-CO_3^- species. These species are reduced at negative potentials (via a two-proton and two-electron process) to form $\text{HC}(\text{OH})_2\text{O}^-$ intermediates, which are further released as HCOOH from the electrode interface [22,59]. Furthermore, the influence of a higher concentration of $\text{In}(\text{OH})_3$ in $\text{In}_{50}/\text{C}_{50}$ seems to predominate over the decrease observed in the particle size for the $\text{In}_{20}/\text{C}_{80}$ in terms of current densities. In addition, it can be also observed in Figure 6a,b that the onset potential at which the CO_2 reduction takes place for the carbon supported catalysts shift to less negative values, which is a clear advantage concerning electric consumption saving issues.

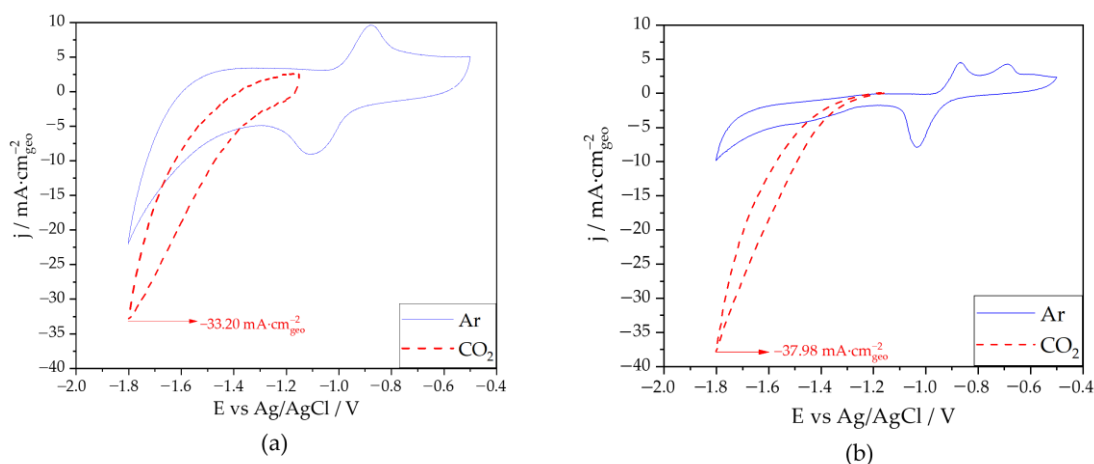


Figure 6. Cyclic voltammograms obtained in Ar (solid lines) and CO_2 (dashed lines) saturated solutions (KHCO_3 0.5 M + KCl 0.45 M) for: (a) $\text{In}_{20}/\text{C}_{80}$ and (b) $\text{In}_{50}/\text{C}_{50}$ NPs. Scan rate $50 \text{ mV}\cdot\text{s}^{-1}$.

Table 1. Current densities ($\text{mA}\cdot\text{cm}^{-2}$) of the different catalysts studied obtained in a CO_2 saturated solution.

Catalyst	Particle Size (nm)	Current Density at $-1.8 \text{ V vs. Ag/AgCl}$ ($\text{mA}\cdot\text{cm}_{\text{geo}}^{-2}$)	Onset Potential of CO_2RR (V) vs. Ag/AgCl
In foil	-	-10.71	-1.25
$\text{In}_{\text{H}_2\text{O}}$	35.95	-12.08	-1.35
In_{KOH}	38.39	-15.20	-1.42
$\text{In}_{20}/\text{C}_{80}$	30.67	-33.20	-1.20
$\text{In}_{50}/\text{C}_{50}$	36.47	-37.98	-1.20

3.2.3. Effect of the Applied Potential

The CO_2RR performance of In_{KOH} , $\text{In}_{20}/\text{C}_{80}$ and $\text{In}_{50}/\text{C}_{50}$ was screened in a potential range between -1.4 V and $-1.7 \text{ V vs. Ag/AgCl}$ in a H-cell under continuous CO_2 bubbling in a solution of 0.5 M KHCO_3 and 0.45 M KCl . As shown in Figure 7a–c, formate was the main product in all cases. There is a voltage window (from -1.40 to -1.50 V) over which formate can be generated with very high FE values in all cases. Particularly, $\text{In}_{50}/\text{C}_{50}$ exhibited the highest Faradaic efficiency towards formate at any cell potential, with values near 100% at -1.4 V and -1.5 V , and with a slight decrease (97%) at $-1.6 \text{ V vs. Ag/AgCl}$. The FE to formate decreased as the voltage became more negative, particularly for the In_{KOH} and $\text{In}_{20}/\text{C}_{80}$ samples, probably due to the generation of hydrogen via HER at the high negative voltages. The $\text{In}_{50}/\text{C}_{50}$ sample also showed higher current density values than the rest of samples over a wide range of potentials.

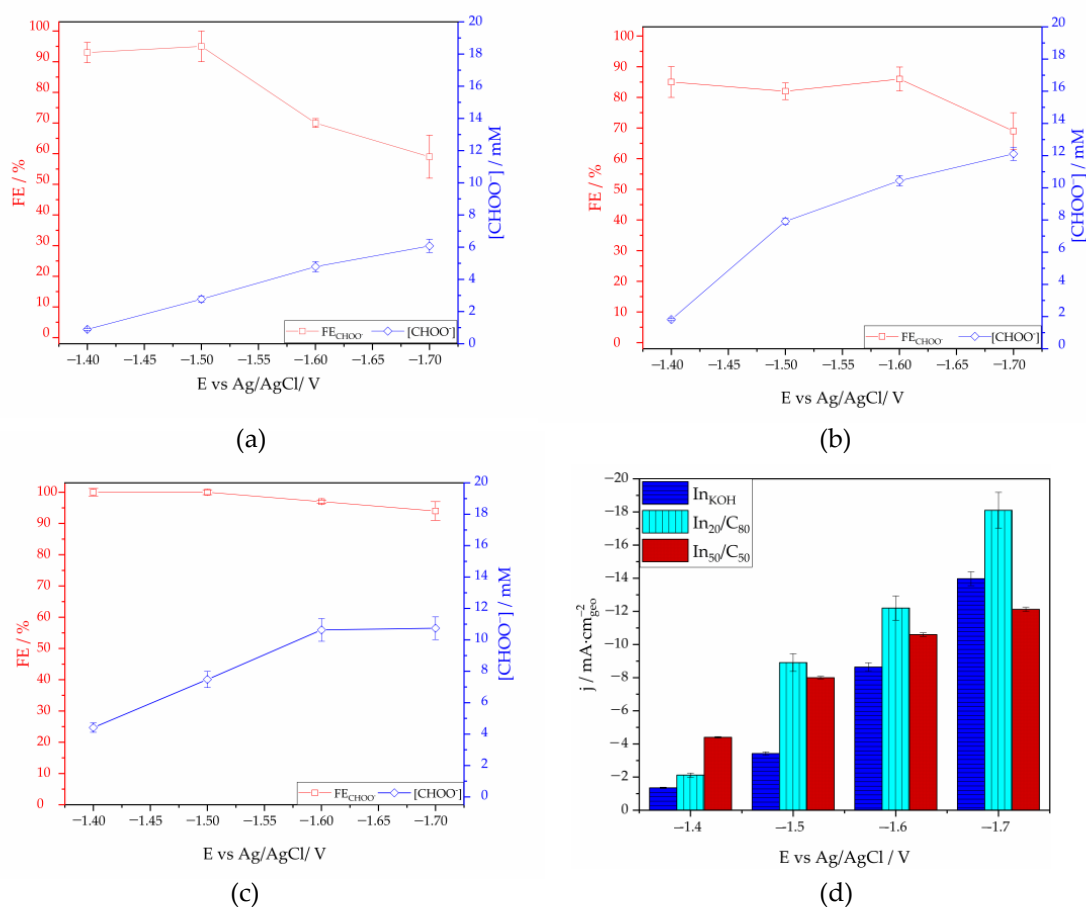


Figure 7. Faradaic efficiency to formate vs. cathodic potential and mM of formate produced for: (a) In_{KOH} ; (b) $\text{In}_{20}/\text{C}_{80}$; (c) $\text{In}_{50}/\text{C}_{50}$ catalyst; and (d) average current densities as a function of the potential.

As mentioned previously, the higher FE to formate observed for $\text{In}_{50}/\text{C}_{50}$ can be attributed, among other aspects, to the presence of surface $\text{In}(\text{OH})_3$ species leading to the formation of essential intermediates for formate production. In particular, at -1.6 V, $\text{In}_{50}/\text{C}_{50}$ catalyst demonstrated approximately 28% of FE increase in comparison with In_{KOH} , and almost 10.5% with $\text{In}_{20}/\text{C}_{80}$. Analyzing the total current densities as a function of the potential (Figure 7d) it can be observed that In_{KOH} exhibit an obviously lower FE to formate in comparison to the In supported on carbon samples. This can be ascribed to the absence of oxidized species in In_{KOH} , as suggested by XPS results.

The total current density is also higher for $\text{In}_{20}/\text{C}_{80}$ than for $\text{In}_{50}/\text{C}_{50}$ at a potential range between -1.5 V and -1.7 V vs. Ag/AgCl. However, considering FE to formate (lower of 90% at any potential), is probable that the $\text{In}_{20}/\text{C}_{80}$ promotes the HER reaction at any potential due to the low concentration of oxidized species, increasing the total current densities registered. It seems that the higher concentration of carbon facilitates the HER, increasing the total current density, but resulting in a detrimental effect on the formate production. These results are in accordance with that suggested in previous works [22,66].

The optimum catalyst $\text{In}_{50}/\text{C}_{50}$ showed nearly complete selectivity to formate while maintaining an acceptable current density of $10.6 \text{ mA}\cdot\text{cm}^{-2}$. Compared with other In-based catalysts reported in the literature (Table 2), $\text{In}_{50}/\text{C}_{50}$ showed slightly higher FE to formate and comparable current density values.

Table 2. Performance of In-based catalyst in the CO₂RR.

Electrocatalyst	Electrolyte	E (V)	j (mA·cm ⁻²)	FE HCOOH	Ref.
In ₅₀ /C ₅₀	0.5 M KHCO ₃ +0.45 M KCl	−1.6 V vs. Ag/AgCl (−0.96 V vs. RHE)	−10.6	~97%	This work
In/C (mp-in)	0.1 M KHCO ₃	−0.95 V vs. RHE	−29.6	~90%	[24]
In ₂ O ₃ @C	0.5 M KHCO ₃	−0.9 V vs. RHE	−29.5	~88%	[66]
In(OH) ₃ /C	0.5 M K ₂ S ₂ O ₄	−1.1 V vs. RHE	−5.2	~77%	[27]
In/C	0.1 M KHCO ₃	−1.0 V vs. RHE	−1	87.8%	[7]
In	0.1 M KHCO ₃	−1.55 V vs. RHE	5.0	94.9%	[67]
In NPs	0.5 M K ₂ SO ₄	−1.5 V vs. Ag/AgCl	~6.0	~90%	[22]

3.2.4. Electrodes Stability

The durability (stability of the current density as a function of time) of the In nanoparticles (In_{KOH}, In₂₀/C₈₀ and In₅₀/C₅₀) was studied performing long-term electrolysis at different potentials (Figure 8). It is worth mentioning that at −1.4 V, where the current density is almost negligible for In_{KOH} and In₂₀/C₈₀, In₅₀/C₅₀ catalyst shows approximately 5 mA·cm⁻². That could be considered as a preliminary indication of the higher activity of this catalyst towards CO₂RR, even at a such low potential as compared to the rest of catalysts analyzed. The In_{KOH} catalyst showed an evident decay on the current density over time at −1.7 V, and even at −1.6 V. This can be explained because of the lower overpotential of the HER for this catalyst. In fact, this is in agreement with the data of FE shown previously, where it could be observed that FE to formate was below 70% (i.e., the hydrogen evolution is taking place markedly). However, In₂₀/C₈₀ and In₅₀/C₅₀ exhibit mainly stable current densities over time except for −1.7 V where, as mentioned, the hydrogen evolution reaction is favored. Hence, a superior behavior can be observed for the supported In NPs. As an example, the current stability for In₂₀/C₈₀ and In₅₀/C₅₀ catalyst remained essentially steady at −1.6 V vs. Ag/AgCl at about −12.5 mA·cm_{geo}⁻² and −10.6 mA_{geo}·cm⁻², respectively, for more than 2.5 h. Evidently, these results proof that the addition of carbon to the In nanoparticles not only increases the activity and selectivity of the CO₂RR, but also has a positive effect into the stability of the catalyst, which is of vital importance for the scalability of the materials to more realistic applications.

The stability of the optimum In₅₀/C₅₀ catalysts was further evaluated by performing SEM elemental mapping for In and EDS measurements before and after 2.5 h of reaction. As shown in Figure 9a,c, In remained uniformly distributed on the electrode surface after reaction, with no evidence of agglomerations of significant losses. Moreover, the EDS measurements before and after reaction (Figure 9b,d) were very similar, indicating that the electrode remained stable after reaction.

On the other hand, HR-TEM analyses were carried out to corroborate the presence of planes ascribed with In⁺³ species by measuring the lattice fringe spacings in the particles deposited on the electrode after 2.5 h of reaction. As shown in Figure 10a, several lattice fringe spacings inside and around the deposited In particle can be observed. These lattice spacings at different points of the particle revealed values of ca. 0.28 nm and 0.31 nm (Figure 10b–e), characteristics of the planes (220) and (121) planes of In(OH)₃, respectively. These results are line with the results exposed in Section 3.1.3. Additionally, the lattice fringe around 0.31 nm could be indexed to (121) plane of In(OH)₃. These results suggest that oxidized In species remained stable as active sites during the reaction.

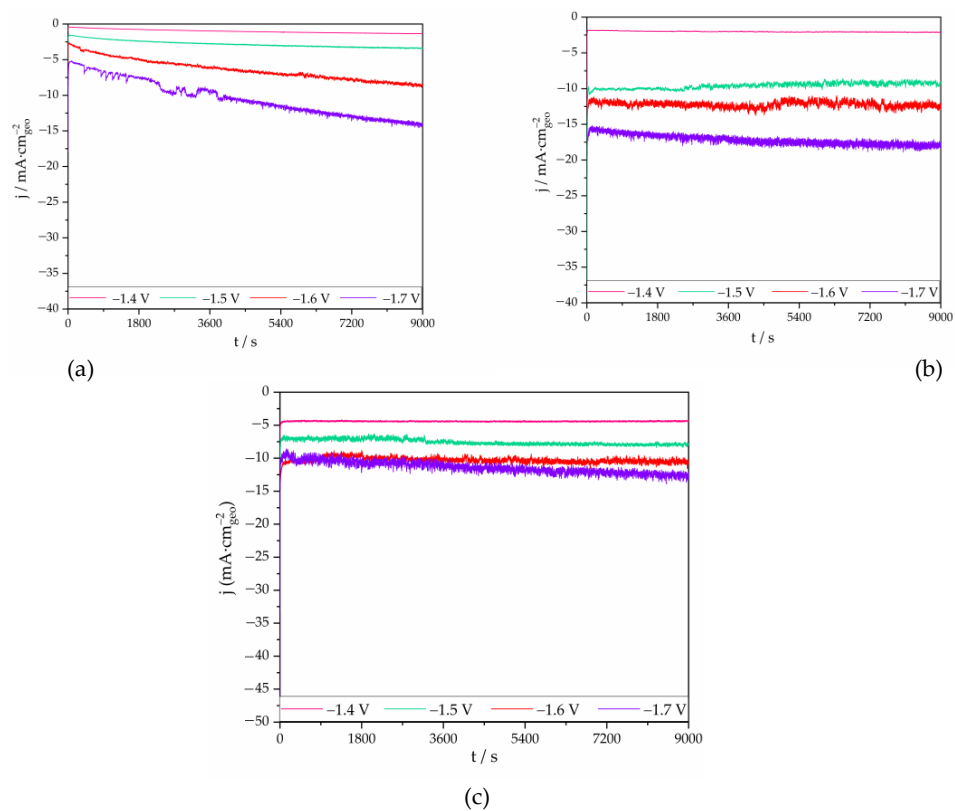


Figure 8. Chronoamperometric measurements at -1.4, -1.5, -1.6 and -1.7 V vs. Ag/AgCl, for: (a) InKOH ; (b) $\text{In}_{20}/\text{C}_{80}$; (c) $\text{In}_{50}/\text{C}_{50}$ catalyst.

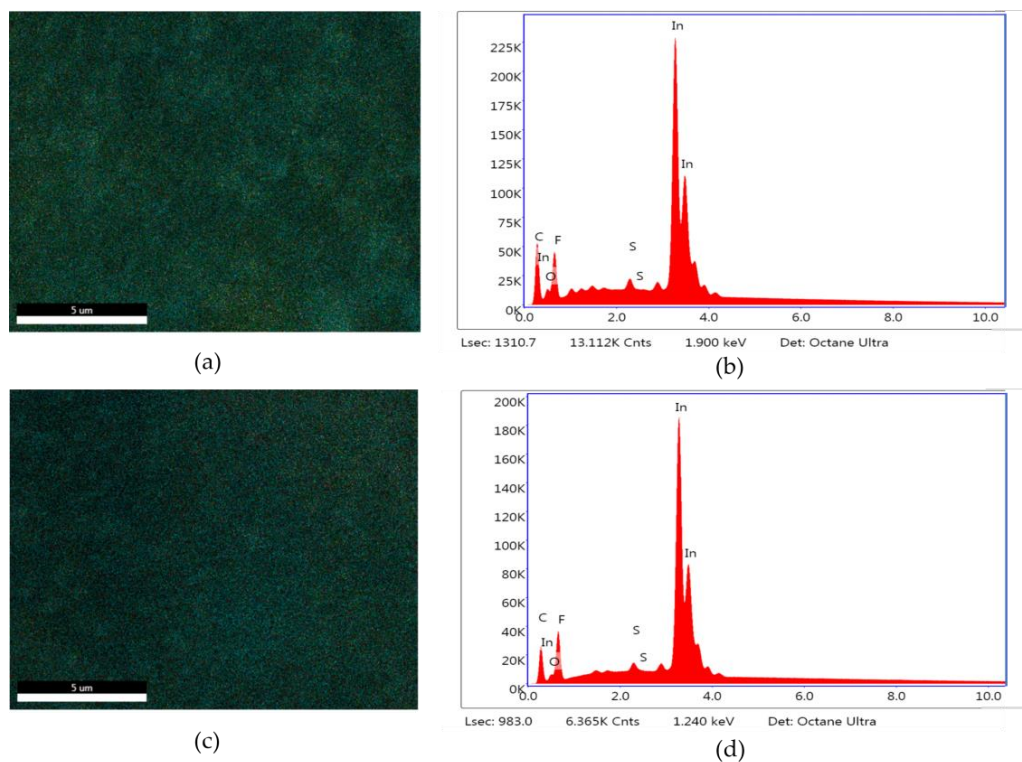


Figure 9. Pre-electrolysis: (a) In distribution mapping of the fresh $\text{In}_{50}/\text{C}_{50}$ electrode surface; (b) EDS measurements of the fresh $\text{In}_{50}/\text{C}_{50}$ electrode; post-electrolysis: (c) In distribution mapping of $\text{In}_{50}/\text{C}_{50}$ electrode surface after CO_2RR ; (d) EDS measurements of the $\text{In}_{50}/\text{C}_{50}$ electrode after CO_2RR .

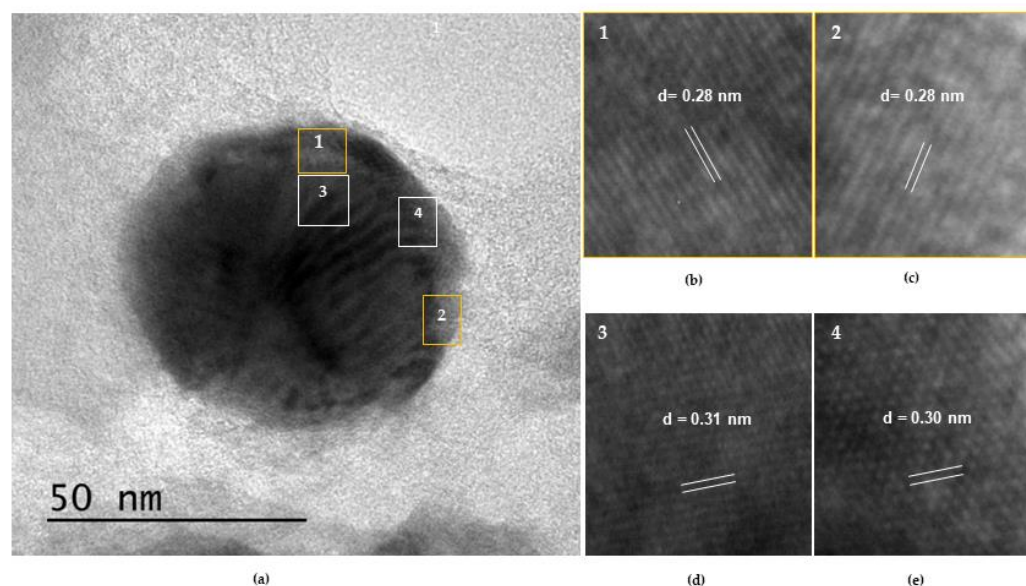


Figure 10. (a) HR-TEM micrograph of particle deposited on $\text{In}_{50}/\text{C}_{50}$ electrode, measure after 2.5 h of electrolysis. (b–e) detail of lattice fringe spacings on spherical nanoparticle.

Additionally, the surface estate of the electrode was studied by XPS. Figure 11 compares the XPS spectra of the $\text{In}_{50}/\text{C}_{50}$ electrode after reaction with that of $\text{In}_{50}/\text{C}_{50}$ particles before reaction. As shown in Figure 11, the XPS spectra of the electrode after reaction was nearly similar to that of the fresh material. A slight shift between both spectra was observed, which can be ascribed to the interactions on In nanoparticles with the support. Consequently, based on the XPS data, we can infer that the $\text{In}_{50}/\text{C}_{50}$ electrode mostly maintained its initial properties after 2.5 h of electrochemical reaction under highly reductive potentials.

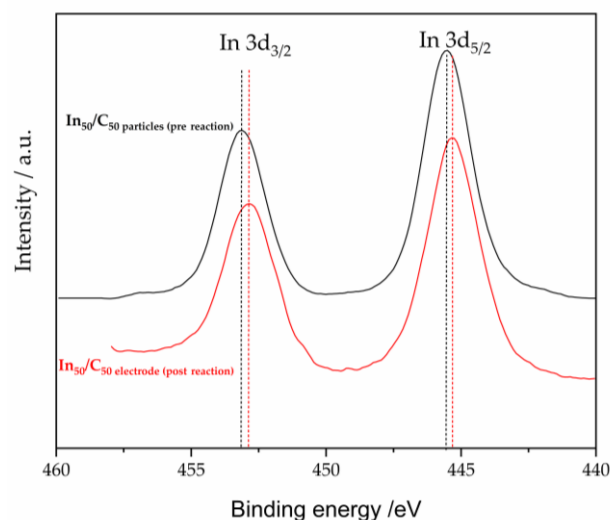


Figure 11. XPS spectra of In 3d for $\text{In}_{50}/\text{C}_{50}$ NPs pre reaction and electrode post reaction.

4. Conclusions

In this study, a simple and scalable method to obtain heterogeneous indium nanoparticles and carbon-supported indium nanoparticles under mild conditions is described in detail. These samples were tested in the electroreduction of CO_2 reaction. Physicochemical characterization revealed all the samples to be composed of In nanoparticles with heterogeneous morphologies, mostly spherical. As revealed by XPS, the carbon-supported samples contained oxidized In species along with reduced In, while the unsupported samples only contained metallic In^0 species. Compared to the unsupported samples, the

carbon-supported materials showed higher electrochemical activities and selectivities to formate. The optimum catalyst obtained by this synthesis method (i.e., In₅₀/C₅₀) showed a high faradaic efficiency to formate (ca. 97%) at -1.6 V vs. Ag/AgCl while showing a stable current density above 10 mA cm^{-2} for more than 2.5 h. The presence of oxidized species in the carbon-supported samples might be responsible for the improved performance of these samples. Additionally, it is recommended to perform more studies to evaluate the effect of different variables on control in morphology and size of NPs, and study in detail the role of carbon support over the catalyst properties.

Supplementary Materials: The following supporting information can be downloaded at: <https://www.mdpi.com/article/10.3390/nano13081304/s1>, Figure S1: XPS survey data for the In₅₀/C₅₀ sample showing the signals for the C 1s, N 1s, O 1s and In 3d levels; Figure S2: CVS curves at scan rates from 10 to 90 $\text{mV}\cdot\text{s}^{-1}$ and capacitive current density against the scan rates and capacitive double layer (C_{dl}) estimation of of In_{KOH}, In₂₀C₈₀ and In₅₀C₅₀; Figure S3: Cyclic voltammograms normalized by electrochemically active surface area (ECSA) obtained in Ar and CO₂ saturated solutions (KHCO₃ 0.5 M + KCl 0.45 M) for In₂₀/C₈₀ and In₅₀/C₅₀ NPs; Table S1: Double layer capacitance and ECSA calculation of the best materials synthesized: In₂₀C₈₀ and In₅₀C₅₀ [68–70].

Author Contributions: Conceptualization, A.C.P.-S.; methodology, A.C.P.-S.; formal analysis, A.C.P.-S. and M.A.D.-P.; investigation, A.C.P.-S.; data curation, J.P.H.; writing—original draft preparation, A.C.P.-S.; writing—review and editing, A.C.P.-S., M.A.D.-P. and M.A.L.A.; visualization, A.C.P.-S. and M.A.D.-P.; supervision, M.A.D.-P. and J.C.S.-R. All authors have read and agreed to the published version of the manuscript.

Funding: J.C.S.-R. would like to thank the Spanish Ministry of Science and Innovation for financial support through the Ramón y Cajal Program, Grant: RYC-2015-19230 and the Research, Development and Innovation projects program, Project number: PID2019-108453GB-C22.

Data Availability Statement: The data presented in this work is contained within this article or supplementary material. More detail can be requested from the authors.

Acknowledgments: The authors would like to acknowledge the technical support from María Jesús Sayagues de Vega (Materials Sciences Institute of Seville) and Victor Márquez (Center of Excellence on Catalysis and Catalytic Reaction Engineering, Chulalongkorn University).

Conflicts of Interest: The authors declare no conflict of interest.

References

1. Köne, A.I.; Büke, T. Forecasting of CO₂ Emissions from Fuel Combustion Using Trend Analysis. *Renew. Sustain. Energy Rev.* **2010**, *14*, 2906–2915. [[CrossRef](#)]
2. Florides, G.A.; Christodoulides, P. Global Warming and Carbon Dioxide through Sciences. *Environ. Int.* **2009**, *35*, 390–401. [[CrossRef](#)] [[PubMed](#)]
3. Inamuddin, R.B.; Ahamed, M.I.; Khan, A. (Eds.) Carbon Dioxide Utilization to Sustainable Energy and Fuels. In *Advances in Science, Technology & Innovation*; Springer International Publishing: Cham, Switzerland, 2021; ISBN 978-3-030-72876-2.
4. Wickramasinghe, S.; Wang, J.; Morsi, B.; Li, B. Carbon Dioxide Conversion to Nanomaterials: Methods, Applications, and Challenges. *Energy Fuels* **2021**, *35*, 11820–11834. [[CrossRef](#)]
5. Jiang, X.; Nie, X.; Guo, X.; Song, C.; Chen, J.G. Recent Advances in Carbon Dioxide Hydrogenation to Methanol via Heterogeneous Catalysis. *Chem. Rev.* **2020**, *120*, 7984–8034. [[CrossRef](#)] [[PubMed](#)]
6. Gao, S.; Wei, T.; Sun, J.; Liu, Q.; Ma, D.; Liu, W.; Zhang, S.; Luo, J.; Liu, X. Atomically Dispersed Metal-Based Catalysts for Zn–CO₂ Batteries. *Small Struct.* **2022**, *3*, 2200086. [[CrossRef](#)]
7. Liu, W.; Feng, J.; Wei, T.; Liu, Q.; Zhang, S.; Luo, Y.; Luo, J.; Liu, X. Active-Site and Interface Engineering of Cathode Materials for Aqueous Zn–Gas Batteries. *Nano Res.* **2022**, *16*, 2325–2346. [[CrossRef](#)]
8. Lu, Q.; Jiao, F. Electrochemical CO₂ Reduction: Electrocatalyst, Reaction Mechanism, and Process Engineering. *Nano Energy* **2016**, *29*, 439–456. [[CrossRef](#)]
9. Lu, X.; Leung, D.Y.C.; Wang, H.; Leung, M.K.H.; Xuan, J. Electrochemical Reduction of Carbon Dioxide to Formic Acid. *ChemElectroChem* **2014**, *1*, 836–849. [[CrossRef](#)]
10. Burke, L.; Healy, J.; Burke, L.D.; Roche, M.C.B.; Electroanal Chem, J.; Roche, M.B.; Scannel, R.; Ahern, M.J.G.; McCarthy, M.M.; Borodzinski, J.; et al. *Atlas of Electrochemical Equilibria in Aqueous Solutions*; Pergamon Press: Oxford, UK, 1992; Volume 139.

11. Zheng, Y.; Vasileff, A.; Zhou, X.; Jiao, Y.; Jaroniec, M.; Qiao, S.Z. Understanding the Roadmap for Electrochemical Reduction of CO₂ to Multi-Carbon Oxygenates and Hydrocarbons on Copper-Based Catalysts. *J. Am. Chem. Soc.* **2019**, *141*, 7646–7659. [[CrossRef](#)]
12. Fan, L.; Xia, C.; Yang, F.; Wang, J.; Wang, H.; Lu, Y. Strategies in Catalysts and Electrolyzer Design for Electrochemical CO₂ Reduction toward C₂₊ Products. *Sci. Adv.* **2020**, *6*, eaay3111. [[CrossRef](#)]
13. Wei, T.; Zhang, S.; Liu, Q.; Qiu, Y.; Luo, J.; Liu, X. Oxygen Vacancy-Rich Amorphous Copper Oxide Enables Highly Selective Electroreduction of Carbon Dioxide to Ethylene. *Wuli Huaxue Xuebao Acta Physico-Chimica Sinica* **2023**, *39*, 2207026. [[CrossRef](#)]
14. Müller, K.; Brooks, K.; Autrey, T. Hydrogen Storage in Formic Acid: A Comparison of Process Options. *Energy Fuels* **2017**, *31*, 12603–12611. [[CrossRef](#)]
15. Yang, W.; Dastafkan, K.; Jia, C.; Zhao, C. Design of Electrocatalysts and Electrochemical Cells for Carbon Dioxide Reduction Reactions. *Adv. Mater. Technol.* **2018**, *3*, 1700377. [[CrossRef](#)]
16. Benson, E.E.; Kubiak, C.P.; Sathrum, A.J.; Smieja, J.M. Electrocatalytic and Homogeneous Approaches to Conversion of CO₂ to Liquid Fuels. *Chem. Soc. Rev.* **2009**, *38*, 89–99. [[CrossRef](#)]
17. Hou, X.; Ding, J.; Liu, W.; Zhang, S.; Luo, J.; Liu, X. Asymmetric Coordination Environment Engineering of Atomic Catalysts for CO₂ Reduction. *Nanomaterials* **2023**, *13*, 309. [[CrossRef](#)] [[PubMed](#)]
18. Zhu, D.D.; Liu, J.L.; Qiao, S.Z. Recent Advances in Inorganic Heterogeneous Electrocatalysts for Reduction of Carbon Dioxide. *Adv. Mater.* **2016**, *28*, 3423–3452. [[CrossRef](#)]
19. Wang, Z.L.; Li, C.; Yamauchi, Y. Nanostructured Nonprecious Metal Catalysts for Electrochemical Reduction of Carbon Dioxide. *Nano Today* **2016**, *11*, 373–391. [[CrossRef](#)]
20. Hori, Y.; Suzuki, S. Cathodic Reduction of Carbon Dioxide for Energy Storage. *J. Res. Inst. Catalysis Hokkaido Univ.* **1983**, *30*, 81–82.
21. Li, J.; Zhu, M.; Han, Y.F. Recent Advances in Electrochemical CO₂ Reduction on Indium-Based Catalysts. *ChemCatChem* **2021**, *13*, 514–531. [[CrossRef](#)]
22. White, J.L.; Bocarsly, A.B. Enhanced Carbon Dioxide Reduction Activity on Indium-Based Nanoparticles. *J. Electrochem. Soc.* **2016**, *163*, H410–H416. [[CrossRef](#)]
23. Ding, C.; Li, A.; Lu, S.M.; Zhang, H.; Li, C. In Situ Electrodeposited Indium Nanocrystals for Efficient CO₂ Reduction to CO with Low Overpotential. *ACS Catal.* **2016**, *6*, 6438–6443. [[CrossRef](#)]
24. Xiao, L.; Liu, X.; Zhou, R.; Zhang, T.; Zhou, R.; Ouyang, B.; Kan, E.; Cullen, P.J.; Ostrikov, K.K.; Tu, X. Facile Synthesis of High-Performance Indium Nanocrystals for Selective CO₂-to-Formate Electroreduction. *Energy Convers. Manag.* **2021**, *231*, 113847. [[CrossRef](#)]
25. Zhang, A.; Liang, Y.; Li, H.; Zhao, X.; Chen, Y.; Zhang, B.; Zhu, W.; Zeng, J. Harmonizing the Electronic Structures of the Adsorbate and Catalysts for Efficient CO₂ Reduction. *Nano Lett.* **2019**, *19*, 6547–6553. [[CrossRef](#)] [[PubMed](#)]
26. Jang, Y.J.; Lee, J.; Kim, J.H.; Lee, B.J.; Lee, J.S. One-Dimensional CuIn Alloy Nanowires as a Robust and Efficient Electrocatalyst for Selective CO₂-to-CO Conversion. *J. Power Sources* **2018**, *378*, 412–417. [[CrossRef](#)]
27. Rabiee, A.; Nematollahi, D. Electrochemical Reduction of CO₂ to Formate Ion Using Nanocubic Mesoporous In(OH)₃/Carbon Black System. *Mater. Chem. Phys.* **2017**, *193*, 109–116. [[CrossRef](#)]
28. Hoffman, Z.B.; Gray, T.S.; Moraveck, K.B.; Gunnoe, T.B.; Zangari, G. Electrochemical Reduction of Carbon Dioxide to Syngas and Formate at Dendritic Copper-Indium Electrocatalysts. *ACS Catal.* **2017**, *7*, 5381–5390. [[CrossRef](#)]
29. Xia, Z.; Freeman, M.; Zhang, D.; Yang, B.; Lei, L.; Li, Z.; Hou, Y. Highly Selective Electrochemical Conversion of CO₂ to HCOOH on Dendritic Indium Foams. *ChemElectroChem* **2018**, *5*, 253–259. [[CrossRef](#)]
30. Wang, M.; Ren, X.; Yuan, G.; Niu, X.; Xu, Q.; Gao, W.; Zhu, S.; Wang, Q. Selective Electroreduction of CO₂ to CO over Co-Electrodeposited Dendritic Core-Shell Indium-Doped Cu@Cu₂O Catalyst. *J. CO₂ Util.* **2020**, *37*, 204–212. [[CrossRef](#)]
31. Hu, S.; Jin, L.; Si, W.; Wang, B.; Zhu, M. Sulfur Vacancies Enriched 2D ZnIn₂S₄ Nanosheets for Improving Photoelectrochemical Performance. *Catalysts* **2022**, *12*, 400. [[CrossRef](#)]
32. Gao, S.; Sun, Z.; Liu, W.; Jiao, X.; Zu, X.; Hu, Q.; Sun, Y.; Yao, T.; Zhang, W.; Wei, S.; et al. Atomic Layer Confined Vacancies for Atomic-Level Insights into Carbon Dioxide Electroreduction. *Nat. Commun.* **2017**, *8*, 14503. [[CrossRef](#)]
33. Zhang, J.; Yin, R.; Shao, Q.; Zhu, T.; Huang, X. Oxygen Vacancies in Amorphous InO_x Nanoribbons Enhance CO₂ Adsorption and Activation for CO₂ Electroreduction. *Angew. Chem.* **2019**, *131*, 5665–5669. [[CrossRef](#)]
34. Wang, J.; Wang, G.; Wu, H.; Liu, F.; Ren, X.; Wang, Y.; Cao, Y.; Lu, Q.; Zheng, X.; Han, X.; et al. Correlating the Crystal Structure and Facet of Indium Oxides with Their Activities for CO₂ Electroreduction. *Fundam. Res.* **2022**; *in press*. [[CrossRef](#)]
35. Yang, W.; Zhao, Y.; Chen, S.; Ren, W.; Chen, X.; Jia, C.; Su, Z.; Wang, Y.; Zhao, C. Defective Indium/Indium Oxide Heterostructures for Highly Selective Carbon Dioxide Electrocatalysis. *Inorg. Chem.* **2020**, *59*, 12437–12444. [[CrossRef](#)]
36. Bin Li, W.; Yu, C.; Tan, X.Y.; Cui, S.; Zhang, Y.F.; Qiu, J.S. Recent Advances in the Electroreduction of Carbon Dioxide to Formic Acid over Carbon-Based Materials. *Xinxing Tan. Cailiao/New. Carbon. Mater.* **2022**, *37*, 277–289.
37. Minh Trung, H.; Duy Thien, N.; Thi Lien, D.; Ngoc Long, N.; van Vu, L. Synthesis and Characterization of Indium Nanoparticles. *VNU J. Sci. Math. Phys.* **2011**, *27*, 3.
38. Bitar, Z.; Fecant, A.; Trela-Baudot, E.; Chardon-Noblat, S.; Pasquier, D. Electrocatalytic Reduction of Carbon Dioxide on Indium Coated Gas Diffusion Electrodes-Comparison with Indium Foil. *Appl. Catal. B* **2016**, *189*, 172–180. [[CrossRef](#)]

39. Bartlett, P.N.; Cook, D.; de Groot, C.H.; Hector, A.L.; Huang, R.; Jolleys, A.; Kissling, G.P.; Levason, W.; Pearce, S.J.; Reid, G. Non-Aqueous Electrodeposition of p-Block Metals and Metalloids from Halometallate Salts. *RSC Adv.* **2013**, *3*, 15645–15654. [[CrossRef](#)]
40. Zhao, Y.; Zhang, Z.; Dang, H. A Novel Solution Route for Preparing Indium Nanoparticles. *J. Phys. Chem. B* **2003**, *107*, 7574–7576. [[CrossRef](#)]
41. Wang, Y.; Nguyen, T.S.; Liu, X.; Wang, X. Novel Palladium-Lead (Pd-Pb/C) Bimetallic Catalysts for Electrooxidation of Ethanol in Alkaline Media. *J. Power Sources* **2010**, *195*, 2619–2622. [[CrossRef](#)]
42. Gu, L.; Dong, Y.; Zhang, Y.; Wang, B.; Yuan, Q.; Du, H.; Zhao, J. Insights into the Role of an Fe-N Active Site in the Oxygen Reduction Reaction on Carbon-Supported Supramolecular Catalysts. *RSC Adv.* **2020**, *10*, 8709–8716. [[CrossRef](#)]
43. Holzwarth, U.; Gibson, N. The Scherrer Equation versus the “Debye-Scherrer Equation”. *Nat. Nanotechnol.* **2011**, *6*, 534. [[CrossRef](#)] [[PubMed](#)]
44. Moulder, J.F.; Stickle, W.F.; Sobol, P.E.; Bomben, K.D.; Chastain, J. *Handbook of X-ray Photoelectron Spectroscopy A Reference Book of Standard Spectra for Identification and Interpretation of XPS Data*; Perkin-Elmer Corporation: Eden Prairie, MN, USA, 1992.
45. Hewitt, R.W.; Winograd, N. Oxidation of Polycrystalline Indium Studied by X-Ray Photoelectron Spectroscopy and Static Secondary Ion Mass Spectroscopy. *J. Appl. Phys.* **1980**, *51*, 2620–2624. [[CrossRef](#)]
46. McGuire, G.E.; Schweitzer, G.K.; Thomas, A.C. Study of Core Electron Binding Energies in Some Group IIIa, Vb, and VIb Compounds. *Inorg. Chem.* **1973**, *12*, 2450–2453. [[CrossRef](#)]
47. Wagner, C.D. Chemical Shifts of Auger Lines, and the Auger Parameter. *Faraday Discuss. Chem. Soc.* **1975**, *60*, 291–300. [[CrossRef](#)]
48. Greczynski, G.; Hultman, L. X-Ray Photoelectron Spectroscopy: Towards Reliable Binding Energy Referencing. *Prog. Mater. Sci.* **2020**, *107*, 100591. [[CrossRef](#)]
49. Chen, X.; Wang, X.; Fang, D. A Review on C1s XPS-Spectra for Some Kinds of Carbon Materials. *Fuller. Nanotub. Carbon. Nanostruct.* **2020**, *28*, 1048–1058. [[CrossRef](#)]
50. Yokota, S.; Okumura, K.; Niwa, M. Support Effect of Metal Oxide on Rh Catalysts in the CH₄—CO₂ Reforming Reaction. *Catal. Lett.* **2002**, *84*, 131–134. [[CrossRef](#)]
51. Whang, H.S.; Lim, J.; Choi, M.S.; Lee, J.; Lee, H. Heterogeneous Catalysts for Catalytic CO₂ Conversion into Value-Added Chemicals. *BMC Chem. Eng.* **2019**, *1*, 9. [[CrossRef](#)]
52. Chou, N.H.; Ke, X.; Schiffer, P.; Schaak, R.E. Room-Temperature Chemical Synthesis of Shape-Controlled Indium Nanoparticles. *J. Am. Chem. Soc.* **2008**, *130*, 8140–8141. [[CrossRef](#)]
53. Banerjee, S.; Loza, K.; Meyer-Zaika, W.; Prymak, O.; Epple, M. Structural Evolution of Silver Nanoparticles during Wet-Chemical Synthesis. *Chem. Mater.* **2014**, *26*, 951–957. [[CrossRef](#)]
54. Lu, X.; Yin, L. Porous Indium Oxide Nanorods: Synthesis, Characterization and Gas Sensing Properties. *J. Mater. Sci. Technol.* **2011**, *27*, 680–684. [[CrossRef](#)]
55. Das, R.; Soni, R.K. Synthesis and Surface-Enhanced Raman Scattering of Indium Nanotriangles and Nanowires. *RSC Adv.* **2017**, *7*, 32255–32263. [[CrossRef](#)]
56. Aghazadeh Meshgi, M.; Kriechbaum, M.; Biswas, S.; Holmes, J.D.; Marschner, C. Synthesis of Indium Nanoparticles at Ambient Temperature; Simultaneous Phase Transfer and Ripening. *J. Nanopart. Res.* **2016**, *18*, 363. [[CrossRef](#)] [[PubMed](#)]
57. George, A.; Choudhary, H.K.; Satpati, B.; Mandal, S. Synthesis, Characterization and Optical Properties of Ligand-Protected Indium Nanoparticles. *Phys. Chem. Chem. Phys.* **2015**, *17*, 7109–7113. [[CrossRef](#)]
58. Wang, J.; Zhang, F.; Wang, Y.; Luo, G. Preparation of In(OH)₃ and In₂O₃ Nanorods through a Novel Hydrothermal Method and the Effect of Sn Dopant on Crystal Structures. *Ind. Eng. Chem. Res.* **2018**, *57*, 2882–2889. [[CrossRef](#)]
59. Detweiler, Z.M.; White, J.L.; Bernasek, S.L.; Bocarsly, A.B. Anodized Indium Metal Electrodes for Enhanced Carbon Dioxide Reduction in Aqueous Electrolyte. *Langmuir* **2014**, *30*, 7593–7600. [[CrossRef](#)] [[PubMed](#)]
60. Markovac, V.; Ovrecek, B. Studies of the Electrochemical Kinetics of Indium III. Systems In + InCl₃ and In + Combined Sulfate-Chloride Electrolyte. *J. Electrochem. Soc.* **1996**, *113*, 838.
61. Piercy, R.; Hampson, N.A. The Indium Electrode in Chloride Electrolytes a Kinetic Study. *J. Electroanal. Chem. Interfacial Electrochem* **1975**, *59*, 261–271.
62. Chung, Y.-H.; Lee, C.-W. Electrochemical Behaviors of Indium. *J. Electrochem. Sci. Technol.* **2012**, *3*, 1–13. [[CrossRef](#)]
63. Ávila-Bolívar, B.; Montiel, V.; Solla-Gullón, J. Electrochemical Reduction of CO₂ to Formate on Nanoparticulated Bi–Sn–Sb Electrodes. *ChemElectroChem* **2022**, *9*, e202200272. [[CrossRef](#)]
64. Gao, S.; Lin, Y.; Jiao, X.; Sun, Y.; Luo, Q.; Zhang, W.; Li, D.; Yang, J.; Xie, Y. Partially Oxidized Atomic Cobalt Layers for Carbon Dioxide Electroreduction to Liquid Fuel. *Nature* **2016**, *529*, 68–71. [[CrossRef](#)] [[PubMed](#)]
65. Luo, W.; Xie, W.; Li, M.; Zhang, J.; Züttel, A. 3D Hierarchical Porous Indium Catalyst for Highly Efficient Electroreduction of CO₂. *J. Mater. Chem. A Mater.* **2019**, *7*, 4505–4515. [[CrossRef](#)]
66. Mou, K.; Chen, Z.; Yao, S.; Liu, L. Enhanced Electrochemical Reduction of Carbon Dioxide to Formate with In-Situ Grown Indium-Based Catalysts in an Aqueous Electrolyte. *Electrochim. Acta* **2018**, *289*, 65–71. [[CrossRef](#)]
67. Hori, Y.; Wakebe, H.; Tsukamoto, T.; Koga, O. Electrocatalytic process of CO selectivity in electrochemical reduction of CO₂ at metal electrodes in aqueous media. *Electrochim. Acta* **1994**, *39*, 1833–1839. [[CrossRef](#)]

68. Wang, J.; Ning, S.; Luo, M.; Xiang, D.; Chen, W.; Kang, X.; Jiang, Z.; Chen, S. In-Sn alloy core-shell nanoparticles: In-doped SnOx shell enables high stability and activity towards selective formate production from electrochemical reduction of CO₂. *Appl. Catal. B Environ.* **2021**, *288*, 119979. [[CrossRef](#)]
69. Li, C.W.; Ciston, J.; Kanan, M.W. Electroreduction of carbon monoxide to liquid fuel on oxide-derived nanocrystalline copper. *Nature* **2014**, *508*, 504–507. [[CrossRef](#)] [[PubMed](#)]
70. Zheng, X.; De Luna, P.; García de Arquer, F.P.; Zhang, B.; Becknell, N.; Ross, M.B.; Li, Y.; Banis, M.N.; Li, Y.; Liu, M.; et al. Sulfur-Modulated Tin Sites Enable Highly Selective Electrochemical Reduction of CO₂ to Formate. *Joule* **2017**, *1*, 794–805. [[CrossRef](#)]

Disclaimer/Publisher's Note: The statements, opinions and data contained in all publications are solely those of the individual author(s) and contributor(s) and not of MDPI and/or the editor(s). MDPI and/or the editor(s) disclaim responsibility for any injury to people or property resulting from any ideas, methods, instructions or products referred to in the content.